PHYSICAL REVIEW FLUIDS **4**, 054702 (2019)

Formation of a thin circulation layer in a two-fluid rotating flow

Igor V. Naumov,[1,*] Vladimir G. Glavny,[1] Bulat R. Sharifullin,[1] and Vladimir N. Shtern[2]
[1]*Kutateladze Institute of Thermophysics SB RAS, 630090 Novosibirsk, Russia*
[2]*Shtern Research and Consulting, Houston, Texas 77096, USA*

(Received 24 August 2018; published 13 May 2019)

Recent numerical simulations predict the formation of a thin circulation layer (TCL) near the interface in a steady axisymmetric swirling flow of two immiscible fluids. This phenomenon, of fundamental and practical interest, has not been detected in prior experiments. The current experimental study reveals that the TCL does develop, but in a way which has not been predicted. The flow is driven by the rotating lid in a vertical cylindrical container—a model of a vortex bioreactor. The centrifugal force pushes the upper fluid from the axis to the sidewall near the lid and the fluid goes back to the axis near the interface. This centrifugal circulation (CC) drives the anticentrifugal circulation (AC) of the lower fluid at a slow rotation. As the rotation speeds up, a CC cell emerges below the interface-axis intersection. It expands downward and occupies almost the entire lower-fluid domain while the AC shrinks into a thin ring adjacent to the interface-sidewall intersection. As the interface starts to visibly rise near the axis, a new AC cell emerges below the interface-axis intersection. This cell and the AC ring merge and form the TCL, attached to the entire interface from below. The TCL is observed in a wide range of the lid angular velocity, until the flow becomes unsteady and three-dimensional. The resulting multicellular flow pattern is favorable for efficient mixing in bioreactors.

DOI: 10.1103/PhysRevFluids.4.054702

I. INTRODUCTION

Swirling two-fluid flows recently attracted the attention of researchers due to applications in aerial vortex bioreactors [1–4]. A propeller drives an air flow, which in turn drives a water flow [1]. The air flow transports oxygen, required for tissue growth, to the interface. The oxygen diffuses through the interface and is dissolved in the water. The meridional circulation of water enhances mixing of the dissolved oxygen with other ingredients. Thus the aerial vortex bioreactor provides gentle and fine mixing of ingredients required for efficient growth of proteins, enzymes, vitamins, antibiotics, sensitive embryonic, hybrid, and other medical cells, ferments and supplements for the food industry, and other tissue cultures [2]. The reactor parameters must be carefully adjusted to avoid undesirable effects such as the tearing of cultures by too strong shear stresses [3]. The tearing can occur because flows in vortex reactors have multiple eddies even if the motion is very slow [5–8].

A proper model of an aerial vortex bioreactor is a sealed vertical cylindrical container filled with water and air. The air-water flow is driven by the rotating lid while the other container walls are stationary. The tissue fraction is small compared to that of water and is neglected in the model while the flow features are studied. The simple geometry and well-defined boundary conditions and control parameters are convenient for both experimental and numerical studies. Comparison of numerical and experimental results helps to better understand the mechanisms of numerous eddy metamorphoses [5–8] and the spectacular shapes of the interface [9–14] typical of these flows.

---

[*] Corresponding author: naumov@itp.nsc.ru

TABLE I. Characteristic velocities in oil and glycerin (in mm/s).

Re	ω_R	V_{zo} min	V_{zo} max	V_{zg} max	V_{zg} min
50	61	0	4.83	0	−0.012
100	122	0	11.5	0.001	−0.019
200	244	0	21	0.218	−0.055
300	367	0	30.2	1.28	0
600	734	6.1	17.7	12.2	−5.7
700	856	−0.8	19.5	15.5	−10.1
800	978	−3.9	18.6	22.4	−19.4
1000	1223	0.4	19.2	30.9	−32.6

The most intriguing and important vortex structure, as predicted by the numerical simulations, is a thin circulation layer (TCL) adjacent to the entire interface. The TCL can significantly enhance the transport of oxygen in the lower fluid. The numerical simulations [15] describe how the TCL forms. The rotating lid induces the centrifugal force that pushes the upper fluid to the periphery near the lid, thus driving the meridional centrifugal circulation (CC); the fluid moves downward near the sidewall, converges to the axis near the interface, and moves upward near the axis to the lid vicinity thus closing the loop. The CC of the upper fluid drives the anticentrifugal circulation (AC) of the lower fluid; it converges near the interface, goes downward near the axis, diverges near the bottom, and rises near the sidewall. Such a flow pattern occurs at a slow rotation.

As the rotation intensifies, a new CC cell emerges near the axis-bottom intersection. It expands upward and occupies almost the entire lower-fluid domain except for a thin AC layer—TCL—formed near the interface [15]. This topological transformation occurs in a steady axisymmetric flow which loses its stability at a significantly faster rotation after the TCL is well developed [16]. The TCL serves as a kind of liquid bearing, separating the centrifugal circulations of the upper and lower fluids.

These interesting and practically important features of swirling two-fluid flows have been explored in detail by numerical simulations [15,16]. However, no experimental study has yet been performed exploring the flow patterns in the lower-fluid domain, particularly the TCL formation. The main difficulty is that the lower-fluid motion is significantly slower than the upper-fluid motion (Table I). This leads to problematic velocity measurements and flow visualization.

The first experimental study of a two-fluid swirling flow in a cylindrical container focused on the interface shapes [9]. In a steady axisymmetric air-water laboratory flow, the interface remains nearly horizontal due to the small air-to-water density ratio. In order to observe significant deformations of the interface, air was replaced with silicon oil whose density is slightly smaller than the water density. This modification revealed spectacular bends of the interface, named by the authors as hump, cusp, Mt. Fuji, and bell [9].

Further experiments with a water–soybean-oil flow [10] found similar shapes of the interface and detected vortex breakdown—formation of an AC cell—near the center of the oil domain. The experimental studies [9,10] were limited to visual observations and provided no information concerning velocity and vorticity fields. The first velocity measurements were performed in a water–sunflower-oil flow [17]. The obtained experimental results for the oil velocity profiles at the rotation axis satisfactorily agree with the numerical simulations. Unfortunately, no measurement was successful in the lower fluid (water) as its velocities were too small to be detected in the steady axisymmetric flow [17].

The current study overcomes this limitation by replacing water with a water-glycerin solution (hereafter referred to as "glycerin" for brevity) whose viscosity is close to the oil viscosity and larger than the water viscosity by two orders of magnitude. The density difference for glycerin and oil is around four times the density difference for water and oil; this moderates the interface deformation. The replacement of water with glycerin allows for measuring velocity and visualizing flow patterns

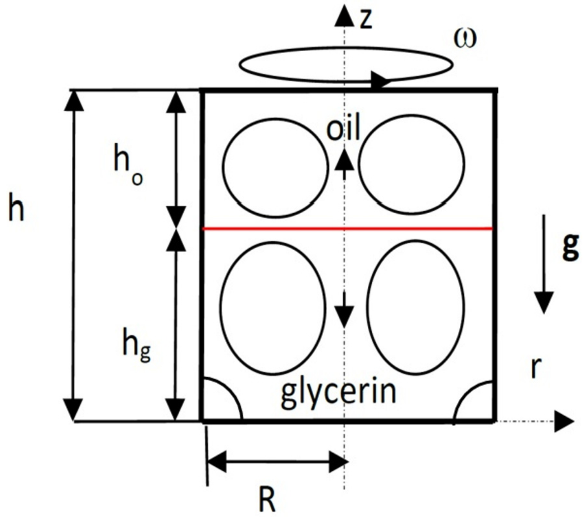

FIG. 1. Problem schematic [22].

in the lower liquid. In particular, the current work provides the first experimental evidence that the TCL does develop in a two-fluid swirling flow and exists in a wide range of the lid rotation speed. The TCL experimental scenario differs with the numerical one [15–17] in that the new cell emerges near the axis-interface intersection and expands downward in the experiment, while it emerges near the bottom and expands upward in the simulations.

In addition to the TCL, the topological patterns of the addressed flow are rich of other circulation cells. Among them are the Moffatt eddies [18–20] and a vortex breakdown bubble [21] emerging and disappearing in the upper fluid. An intriguing feature is a discontinuity of radial velocity occurring at the interface. This phenomenon, recently detected in another study [22], is found here to be an important stage of the TCL development as the rotation intensifies.

In the sections to follow, we briefly formulate the problem (Sec. II) and refer the reader to Ref. [17] for details of the experimental techniques. Section III discusses the experimental results and Sec. IV provides a summary.

II. PROBLEM FORMULATION AND EXPERIMENTAL TECHNIQUE

A. Problem formulation

Figure 1 shows a schematic of the problem which is similar to that in Refs. [17,22]. Two immiscible fluids move in a sealed vertical cylindrical container of radius R and height h. The flow is driven by the lid, rotating with angular velocity ω, while the other container walls are stationary. At rest, the axial extents of the heavy and light fluids are h_g and h_o, respectively; $\mathbf{g}$ is the gravitational acceleration. The scales, R for lengths and ωR for velocities, are used for dimensionless quantities throughout this paper.

Figure 1 also shows a schematic of the steady axisymmetric meridional motion at small Re. The centrifugal force, induced by the lid rotation, drives the meridional centrifugal circulation of the upper fluid: it radially diverges from the axis to the sidewall near the lid, goes down near the sidewall, converges toward the axis near the interface, and goes up to the lid near the axis. The upper-fluid convergence near the interface tends to drive the anticentrifugal circulation of the lower fluid, while the upper-fluid rotation near the interface tends to drive the centrifugal circulation of the lower fluid. Thus the upper-fluid convergence and rotation compete, tending to drive the lower fluid in the opposite directions. This competition generates cells of both circulation directions as Re increases. For small Re, the rotation effect is weaker than the convergence effect because the swirl

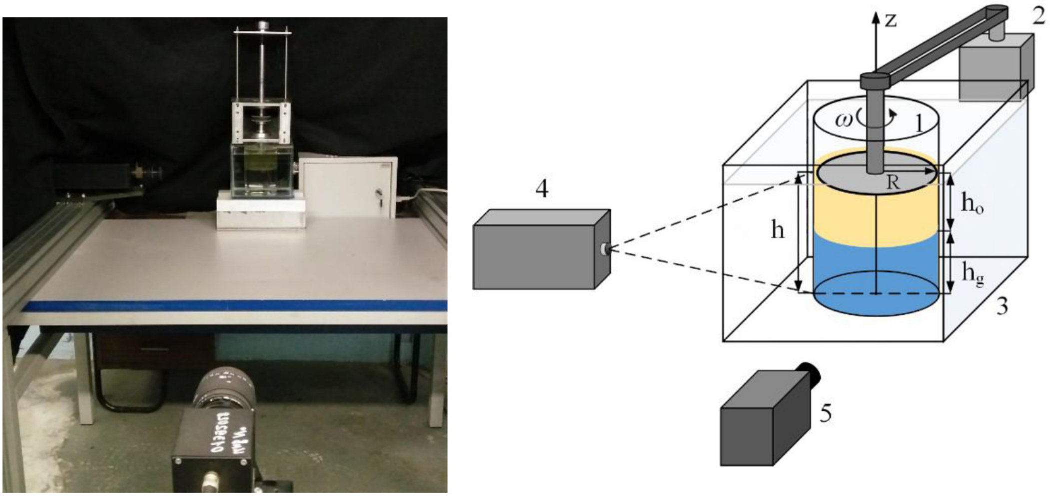

(a)

(b)

FIG. 2. (a) Photo and (b) schematic of the experimental setup [22].

rapidly decays downward of the lid. This leads to the anticentrifugal circulation of the lower fluid as shown in Fig. 1.

The circulation of the lower fluid drives the Moffatt eddies [18] observed in the numerical simulations [5,15] and schematically shown near the bottom-sidewall intersection in Fig. 1. As Re increases, the interface rotation speeds up and causes the development of a new centrifugal-circulation cell of the lower fluid, as discussed in more detail in Sec. III A.

B. Experimental setup and technique

Figure 2 shows a photo and a schematic of the experimental setup which is similar to that in Refs. [17,22]. It consists of a cylindrical container (1), stepping motor DSI-200-2 (2), rectangular box filled with water (3), Nd:YAG pulsed laser POLIS v3.2 (4), and POLIS camera v1.0 (5). The cylindrical container is made of transparent optical glass with the inner radius $R = 45\,\text{mm}$ and height 126 mm. The lid can be positioned at a varying height h [17,22]. The container is filled with glycerin ($0 < z < h_g$) and sunflower oil ($h_g < z < h$); z is the distance from the container bottom and $h = h_g + h_o$. Hereafter subscripts “g” and “o” denote glycerin-water solution and oil. The dimensions are $h = 2.5R$, $h_g = 1.5R$, and $h_o = R$. The glycerin-water (22%–78%) solution is of density $\rho_g = 1208\,\text{kg/m}^3$ and kinematic viscosity $\nu_g = 42.82 \times 10^{-6}\,\text{m}^2/\text{s}$. The sunflower oil is of density $\rho_o = 920\,\text{kg/m}^3$ and viscosity $\nu_o = 54.86 \times 10^{-6}\,\text{m}^2/\text{s}$. Estimated surface tension at the interface is $\sigma = 0.0315\,\text{N/m}$. The interface at rest is shown by the horizontal (red) line in Fig. 1. The flow is kept isothermal at room temperature, 22.6°C. The rotation intensity is characterized by the Reynolds number $\text{Re} = \omega R^2/\nu_o$. The whole cylindrical container was placed inside a rectangular box. The box is made of glass and filled with water to minimize optical aberrations and thermal changes.

The velocity fields are measured with the help of particle image velocimetry (PIV). Polyamide beads, of density $1030\,\text{kg/m}^3$ and diameter around $20\,\mu\text{m}$, are employed as seeding light-scattering particles for both the flow visualization and PIV measurements. The use of PIV provides an instantaneous velocity distribution in the investigated cross section and an instantaneous flow pattern within the two-dimensional plane of a light sheet. As an optical source for the light sheet we used a Nd:YAG pulsed laser POLIS v3.2 with a wavelength of 532 nm, a light sheet thickness of 1 mm, an energy pulse power of 120 mJ, and an operation frequency of 2 Hz. Measurements were performed

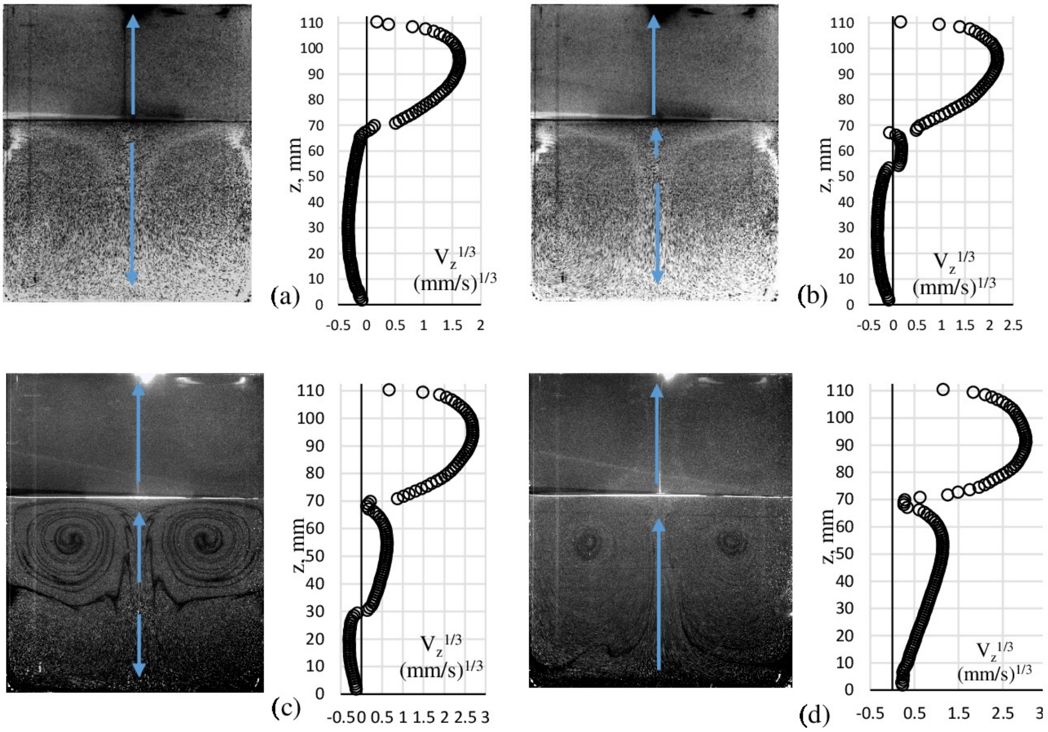

FIG. 3. Photos of PIV images of the meridional motion and profiles of velocity along the axis at (a) Re = 50, (b) Re = 100, (c) Re = 200, and (d) Re = 300 [22].

in a vertical cross section located at the geometric center of the container. Images were recorded by POLIS camera v1.0 with lens Nikon AF 28 mm $f/2.8$D Nikkor. The experimental setup and measurement techniques, used in the current study, are described in more detail in Refs. [13,17].

III. DISCUSSION OF EXPERIMENTAL RESULTS

Table I lists dimensional characteristic velocities. V_z denotes the velocity at the axis; subscripts g and o mean glycerin and oil, respectively; and max and min correspond to the maximal and minimal values. It is instructive to explore the flow by eventually increasing Re starting with its small values. Table I shows that the glycerin velocities are very small compared with the oil velocities for $\mathrm{Re} < 300$. The small glycerin-to-oil velocity ratio is a challenge both for the PIV measurements and for the analysis of the flow pattern in the glycerin domain. This difficulty is overcome by means discussed in more detail next.

A. Development of centrifugal circulation in the lower fluid

Figure 3 shows photos of PIV images of the meridional motion (left, similar to that in Ref. [22]) and velocity distributions along the rotation axis, $V_z(z)$ at $r = 0$ (right), for a few characteristic values of the Reynolds number. The interface is observed in the photos as the horizontal dark and light lanes. The velocity profiles are obtained by postprocessing of the experimental data after averaging of 200 PIV images at a fixed Re. The averaging increases the signal-to-noise ratio. The arrows in the photos indicate the flow direction near the axis. Since the glycerin velocity is very small compared with the oil velocity for these values of Re, we plot $V_z^{1/3}$ to conveniently observe the velocity profiles of both upper and lower fluids in one figure.

At $\mathrm{Re} = 50$, the experimental flow topology is identical to that schematically depicted in Fig. 1. As Fig. 3(a) shows, the velocity at the axis is positive (directed upward) in the upper fluid and negative (directed downward) in the lower fluid. At $\mathrm{Re} = 100$, a small range of positive V_z emerges below the interface-axis intersection, as the plot in Fig. 3(b) shows. This range, marked by the short arrow in the photo of Fig. 3(b), corresponds to a just emerged cell of the glycerin centrifugal circulation. Figure 3(c) shows that this cell occupies approximately the upper half of the glycerin domain at $\mathrm{Re} = 200$. At $\mathrm{Re} = 300$, the centrifugal circulation occupies almost the entire glycerin domain, as Fig. 3(d) shows.

An intriguing physical phenomenon is a slip, which is observed close to the near-axis part of the interface. Figure 4 highlights this slip by combining a schematic of the flow pattern at $\mathrm{Re} = 200$ [Fig. 4(a)] and plots of measured radial velocity V_r (normalized by ωR) as a function of the distance from the axis, r, near the interface ($z = z_\mathrm{i} = 67.5\,\mathrm{mm}$), in oil (open circles, $z = 68\,\mathrm{mm}$), and in glycerin (solid circles, $z = 67\,\mathrm{mm}$) [Figs. 4(b)–4(e)]. Here z_i and z_s are heights at the axis of the interface and the glycerin centrifugal circulation, respectively. The circle size in the plots indicates the measurement accuracy.

Figure 4(b) shows that the oil and glycerin velocities are close at $\mathrm{Re} = 50$ while Figs. 4(c)–4(e) show that the velocities are very different, even having opposite directions at the near-axis part of the interface for $\mathrm{Re} = 100$, 200, and 300. In the oil domain, $V_r \leqslant 0$ at the entire interface, i.e., oil moves from the sidewall to the axis, as the long horizontal arrows indicate above the interface in Fig. 4(a).

In contrast, the radial velocity of glycerin is positive below the near-axis part of interface, as Figs. 4(c)–4(e) show, i.e., glycerin moves there from the axis toward the sidewall, as the long horizontal arrows below the interface indicate in Fig. 4(a). Thus there is a counterflow: oil and glycerin move in the opposite directions along the near-axis part of the interface. This slip can be caused by the difference in the fluid densities and the centrifugal force, which pushes to the periphery glycerin more srtongly than oil. At $\mathrm{Re} = 50$, the swirl rapidly decays downward, making the centrifugal force very weak near the interface. Accordingly, no significant slip is observed in Fig. 4(b). However, the slip develops at larger Re as Figs. 4(c)–4(e) reveal.

The topological transformation of the glycerin flow, illustrated by Figs. 3 and 4, occurs because the increased rotation (factor A) overcomes the effect of the oil meridional centrifugal circulation (factor B) and induces the centrifugal circulation in glycerin as well. Close to the interface, the anticentrifugal circulation of glycerin shrinks into a ring, attached to the sidewall-interface intersection as schematically depicted in Fig. 4(a). This ring, being very thin, is hardly observed in the photos of Figs. 3(c) and 3(d), but is well detected by the ranges of negative glycerin velocity in Figs. 4(d) and 4(e). As Re increases, the competition of factors A and B results in further topological transformations discussed next.

B. Development of a thin circulation layer in the lower fluid

The photos in Fig. 5 show that the interface starts to visibly rise near the axis for $\mathrm{Re} > 300$ and the plots depict the dependence on the height z (in mm) of measured velocity V_z (in mm/s) at the axis. The open (solid) circle symbols correspond to the oil (glycerin) domain in the plots of Fig. 5. At these Re values, the maximal magnitudes of V_z in oil and glycerin become rather close. Therefore, in contrast to Fig. 3, there is no need to plot $V_z^{1/3}$ in Fig. 5.

The positive values of V_z correspond to the centrifugal circulations of oil (above the solid horizontal line, at $z > z_i$) and glycerin (below the dashed horizontal line, at $z < z_\mathrm{s}$). The negative values of V_z correspond to the thin layer of anticentrifugal circulation (TCL) of glycerin in the range $z_\mathrm{s} < z < z_\mathrm{i}$, located between the solid and dashed horizontal lines in the plots of Fig. 5. At $z = z_\mathrm{s}$ and $z = z_\mathrm{i}$, $V_\mathrm{z} = 0$ on the axis.

Figure 6(a) depicts the dependence on Re of the TCL thickness, $z_i - z_s$, at the axis. Figure 6(a) reveals that the TCL emerges at Re close to 300 and its axial extent saturates to the value around

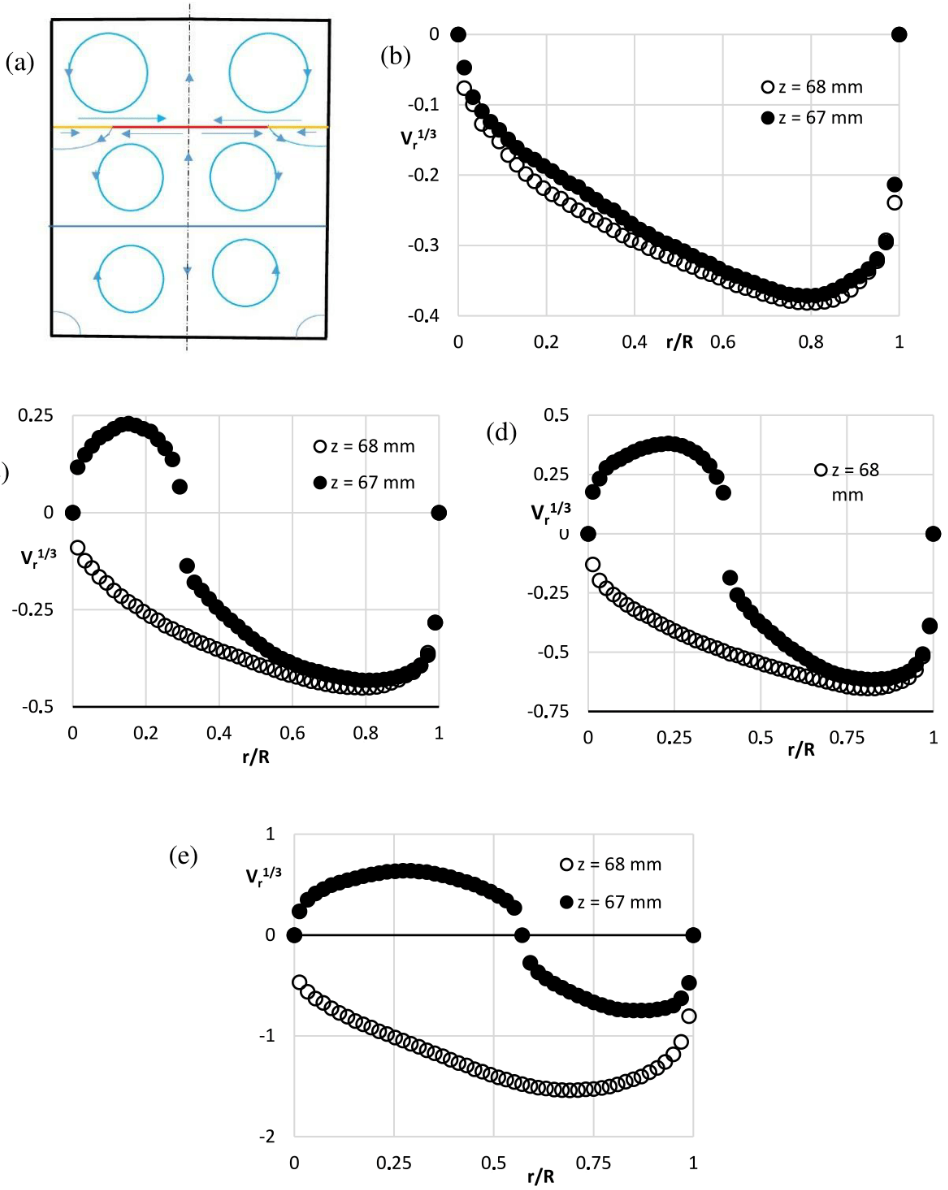

FIG. 4. (a) Schematic of meridional motion at Re = 200 and profiles of radial velocity near the interface in oil (open circles) and glycerin (solid circles) at (b) Re = 50, (c) Re = 100, (d) Re = 200, and (e) Re = 300.

0.1R as Re increases. The square symbols represent the measured values of $z_i - z_s$ while the curve is a trend line in Fig. 6(a); its equation is given there.

Figure 6(b) depicts the dependence on Re of the interface heights at the axis (squares) and at the sidewall (circles). It is interesting that the height at the axis starts to visibly rise at Re around 300, at which the TCL emerges. The interface height at the sidewall starts to visibly drop at Re around 900, at which the TCL axial extent saturates, as Fig. 6(a) illustrates.

Since the PIV geometry is planar and meridional, it only provides measurements of the axial and radial components of velocity. Errors are caused by pixel sizes as well as by displacements

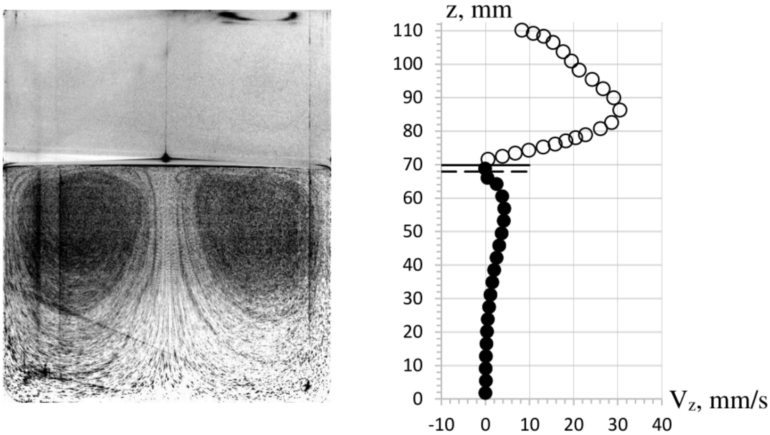

(a) Re = 400 (b)

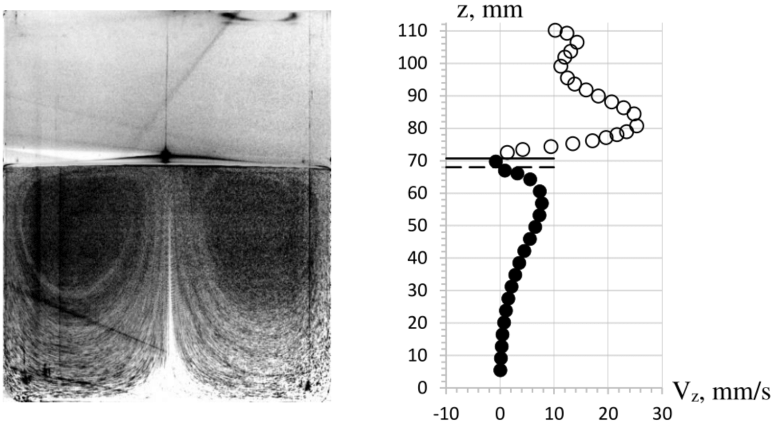

(c) Re = 500 (d)

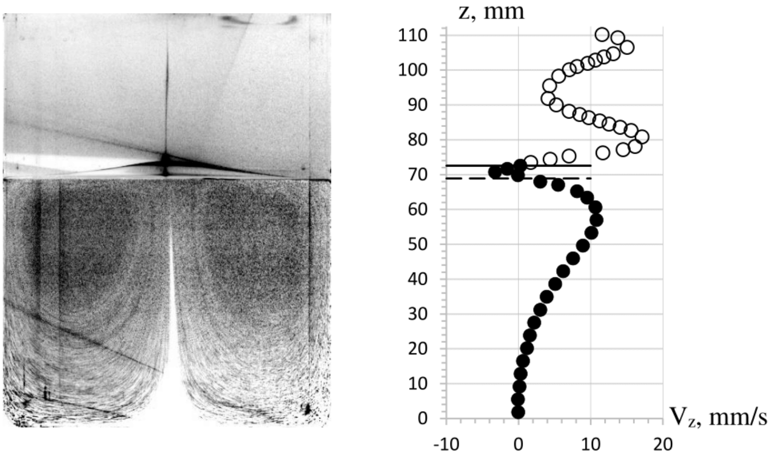

(e) Re = 600 (f)

FIG. 5. Photos of flow patterns (left) and plots of velocity distribution at the axis (right).

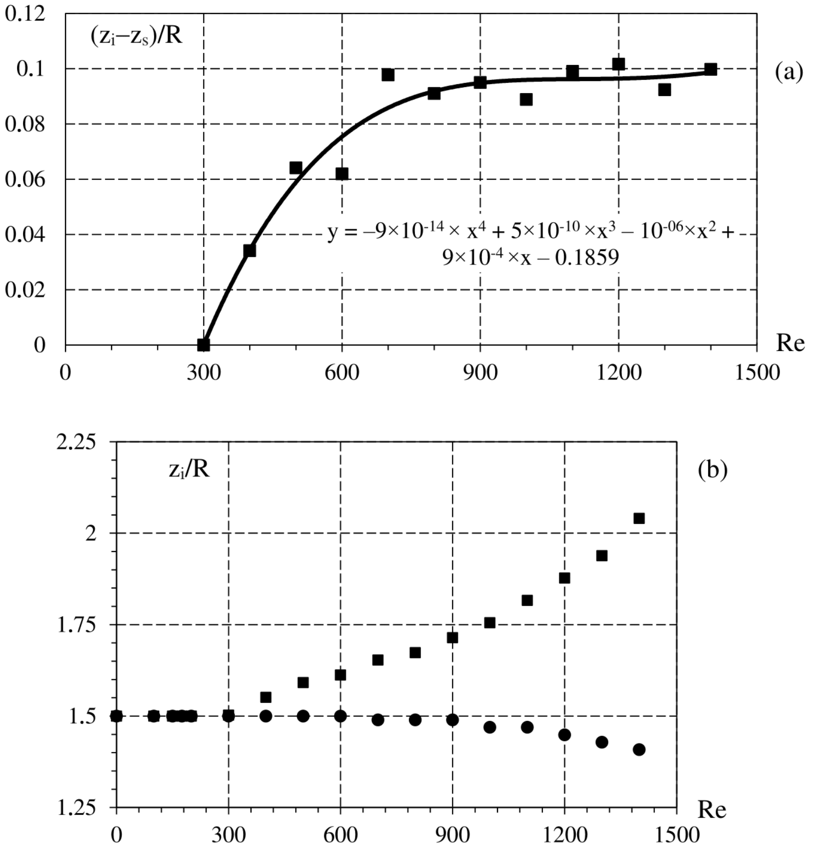

FIG. 6. Dependence on the Reynolds number of (a) the TCL thickness and (b) interface height z_i at the axis (squares) and at the sidewall (circles).

and distortions provided by the cylindrical sidewall. We explore (a) the entire velocity field in the meridional cross section of the cylindrical container and (b) the enlarged near-interface regions with spatial resolutions of 0.115 mm in (a) and 0.038 mm in (b). This leads to velocity errors of 2% and 1%, respectively. Since the flow is stationary and the errors are random, we increase the signal-to-noise ratio by averaging 200 instantaneous velocity fields. Distortions due to the cylindrical sidewall do not significantly affect velocities near the axis while they sometimes cause up to 5% errors of the radial velocity at the periphery. Fortunately, these errors do not significantly affect the profiles shown in Fig. 4. Since these errors are small, their presentation by bars looks odd in the plots. For this reason, we use the circle size to indicate the measurement accuracy. The circle size sometimes is much larger than the error bars, e.g., in Figs. 3, 4, 5, and 7.

C. Vortex breakdown in the oil domain

The next topological change—vortex breakdown (VB)—occurs in the oil flow, as Re further increases. The swirl decay mechanism, generating VB [19,20], starts to work. The centrifugal circulation of oil strengthens and a jetlike boundary layer develops near the sidewall and near the interface. This jet enhances transport of the angular momentum from the lid along the sidewall to the interface and along the interface to the axis. The resulting accumulation of angular momentum forms a tornadolike vortex near the axis-interface intersection. The strengthening centrifugal force enlarges the radial gradient of pressure and thus reduces pressure near the axis-interface intersection.

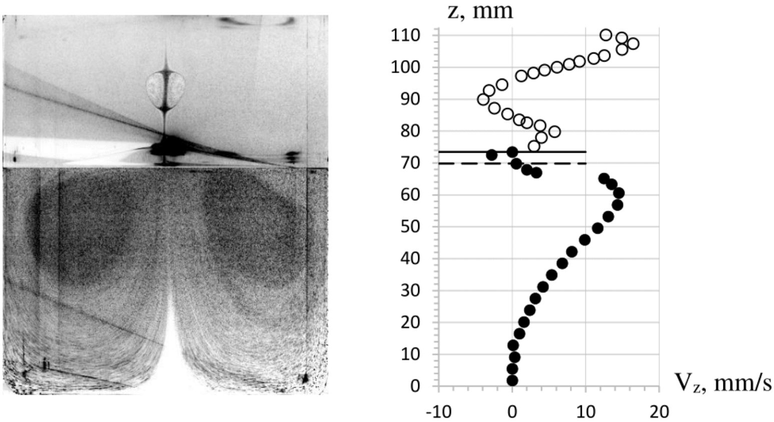

(a) Re = 700 (b)

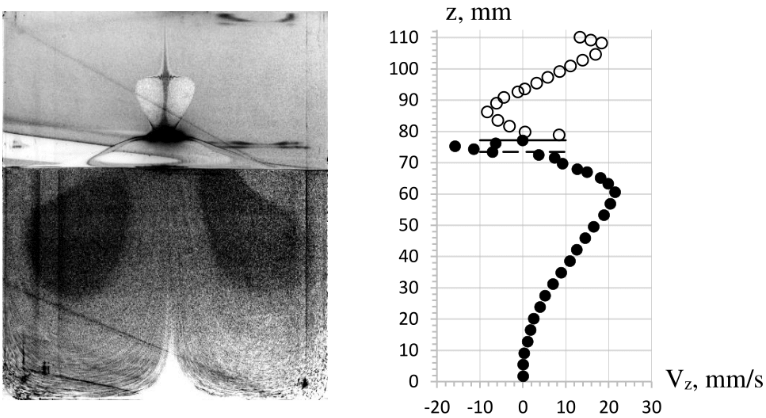

(c) Re = 900 (d)

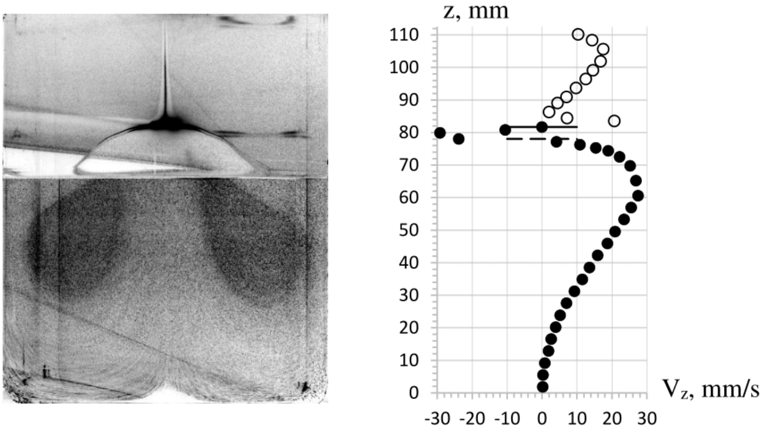

(e) Re = 1100 (f)

FIG. 7. Photos of vortex breakdown bubble in the oil flow and plots of velocity distribution at the axis.

Suction, provided by the reduced pressure, decelerates the near-axis ascending swirling jet and reverses its axial velocity where the jet diverges and its swirl weakens.

First, a local minimum in $V_z(z)$ emerges, which is observed at $\text{Re} = 500$ near $z = 96\,\text{mm}$ in Fig. 5(d). The minimum value decreases at $\text{Re} = 600$, as Fig. 5(f) illustrates, and becomes negative near $z = 90\,\text{mm}$, as Fig. 7(b) shows at $\text{Re} = 700$. The z range of oil negative velocity in Fig. 7(b) corresponds to the axial extent of the cell located near the center of the oil domain in Fig. 7(a). This cell of the anticentrifugal circulation is often referred to as a vortex breakdown bubble (VBB).

Next, the suction attracts the VBB to the interface, as Fig. 7(c) shows at $\text{Re} = 900$. It could be mistakably imagined that the VBB touches the interface in Fig. 7(c). However, Fig. 7(d) destroys this illusion by revealing that the VBB is separated from the interface by a thin oil layer. In this layer, V_z is positive at the axis and its maximal value exceeds 10 mm/s near $z = 80\,\text{mm}$ in Fig. 7(d).

The axial extent of the $V_z > 0$ oil layer, which is small at $\text{Re} = 900$, further diminishes as Re grows. This blocks the transport of the angular momentum to the axis vicinity located below the VBB. The blockage weakens the suction while the oil convergence along the interface strengthens. This weakening suction and enhancing oil convergence kill the VBB. At $\text{Re} = 1100$ there is no VBB in Fig. 7(e), but Fig. 7(f) shows that the positive value of the V_z local minimum near $z = 86\,\text{mm}$ is close to zero. This small value indicates that the VBB disappears at Re being just a little bit less than 1100. Thus, the strengthening (weakening) suction generates (suppresses) the VBB as Re increases. This explains the fold of the VB curve on the (h/R, Re) map for a confined flow [21].

While the VBB emerges, develops, and disappears in oil, the maximal magnitude of V_z at the axis becomes located in glycerin and particularly in the TCL as the last row of Table I and Fig. 7(f) illustrate. This strengthening of TCL meridional flow stimulates the interface transformation from the hump shape to the bell shape as discussed next in more detail.

D. Role of TCL in the interface bell shape

Figure 8 helps understand the role of TCL in the formation of the interface bell shape. The velocity at the axis is directed downward inside the TCL and upward below the TCL. These two near-axis streams collide, turn away from the axis, and form a radially diverging jetlike flow. This flow, located along the TCL lower boundary, approaches the interface, pushes it outward, and thus produces the different slopes of the interface upper (near-axis) and middle (truncated conical) parts, as Fig. 8(a) illustrates at $\text{Re} = 1200$. While Re increases, the velocity magnitudes of the colliding near-axis flows grow, as comparison shows of Figs. 8(b), 8(d), and 8(f).

Accordingly, the radially diverging jetlike flow becomes stronger, causing the development of the bell cap and the bell truncated-conical body well observed in Fig. 8(e) at $\text{Re} = 1400$. For $\text{Re} > 1400$, the flow becomes unsteady and the interface shape becomes asymmetric.

Thus, the steady axisymmetric TCL is observed in the wide range of Re, $300 < \text{Re} < 1400$, and contributes to the development the interface bell shape.

E. Velocity vector fields of meridional motion

Figures 9 and 10 present PIV flow patterns in the meridional cross section at a few characteristic values of the Reynolds number. In order to conveniently observe the patterns and to diminish the effect of random errors, the arrows show velocity vectors normalized by their magnitude, i.e., only the velocity direction.

Figures 9 and 10 show the photos (left) and the PIV visualizations (right) of the meridional motion at $\text{Re} = 50$, 150, 300, 600, 900, and 1300. The PIV pictures are obtained by postprocessing 200 images to increase the signal-to-noise ratio. Figure 9 shows the entire flow domain. Figure 10 only shows the enlarged near-interface regions at the same Re values as those in Fig. 9, but with the PIV camera being focused on the near-interface regions. This provides the better space resolution: 0.33 mm in Fig. 10 compared with 0.8 mm in Fig. 9. Similar flow patterns have been numerically

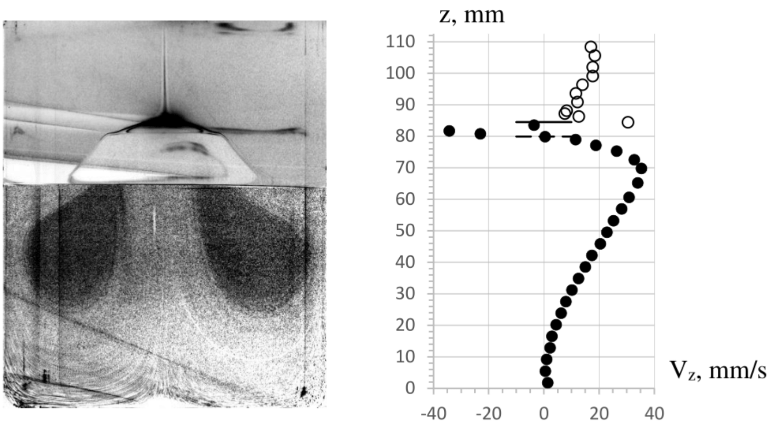

(a) Re = 1200 (b)

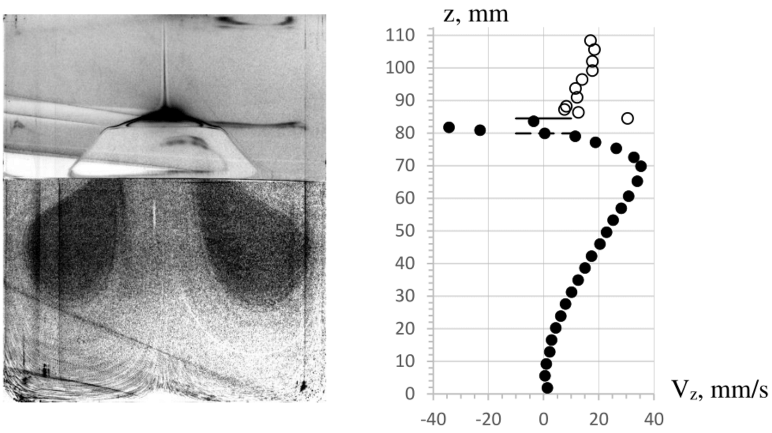

(c) Re = 1300 (d)

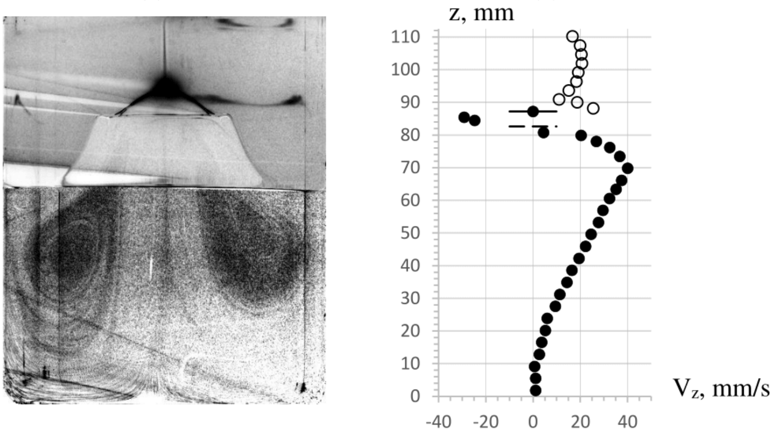

(e) Re = 1400 (f)

FIG. 8. Photos of the bell-shape interface and plots of velocity distribution at the axis.

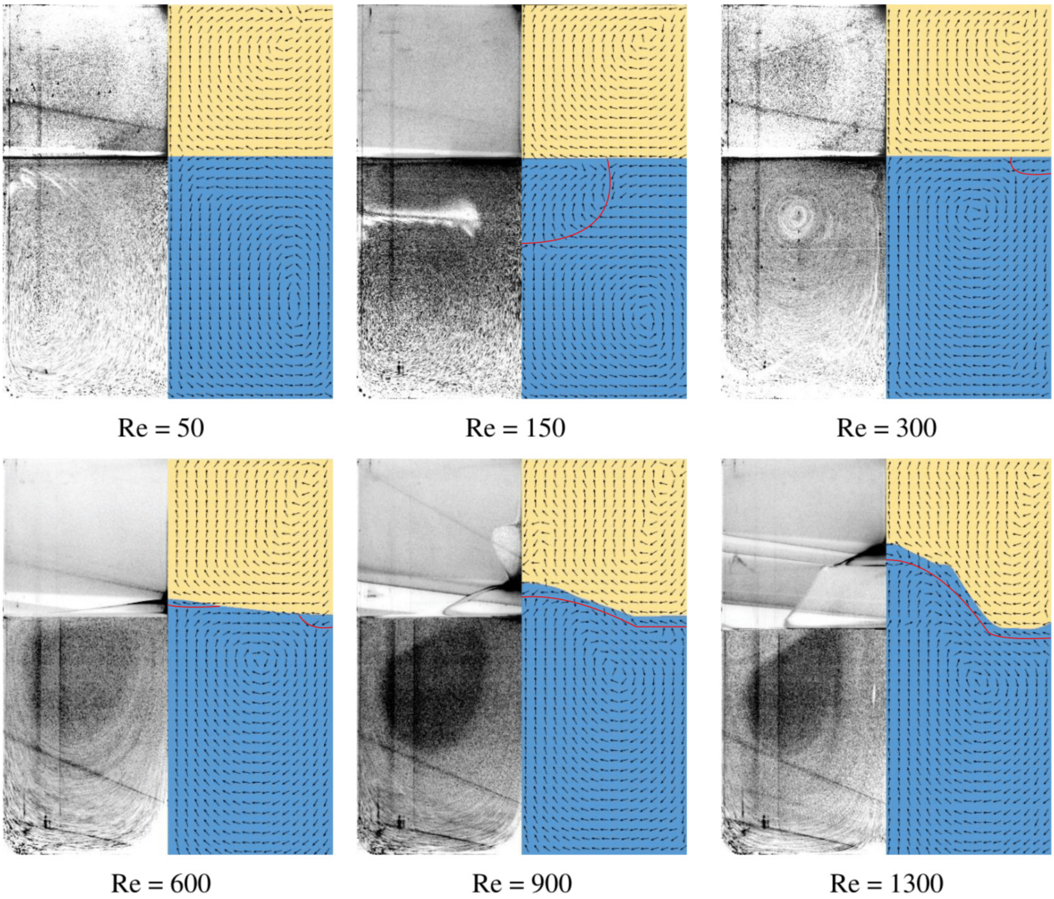

FIG. 9. Photos (left) and PIV images of the meridional flow (right).

simulated [15,16], but no vector field of two-fluid swirling flows has been experimentally obtained in prior studies.

The light (yellow) regions depict the oil flows and the dark (blue) regions depict the glycerin flows in Figs. 9 and 10. Unfortunately, the PIV resolution is poor where the meridional velocity magnitude is small. However, the bulk centrifugal circulations of both oil and glycerin are well observed in Fig. 9.

The emerged cell of centrifugal glycerin circulation near the axis-interface intersection is well visible at Re = 150 in Fig. 9. The red curve roughly separates the glycerin currents directed toward the axis and away from the axis. The reduced anticentrifugal glycerin circulation near the interface-sidewall intersection is observed at Re = 300 in Figs. 9 and 10. At Re = 600, Figs. 9 and 10 show two separated near-interface cells of the anticentrifugal glycerin circulation: the new cell, located near the axis, and the old cell, located near the sidewall. At Re = 900, Figs. 9 and 10 show that these two cells merge, forming the TCL attached to the entire interface from below. The TCL is well visible at Re = 1300 in Fig. 10, which reveals that the TCL axial extent is reduced near the interface bends between its (a) cap and conical and (b) conical and horizontal parts.

Thus, despite some resolution limitations, Figs. 9 and 10 demonstrate the key results of this study: (i) the TCL does develop in the lower-fluid domain, as Re increases, and (ii) the TCL is attached to the entire interface from below for large Re.

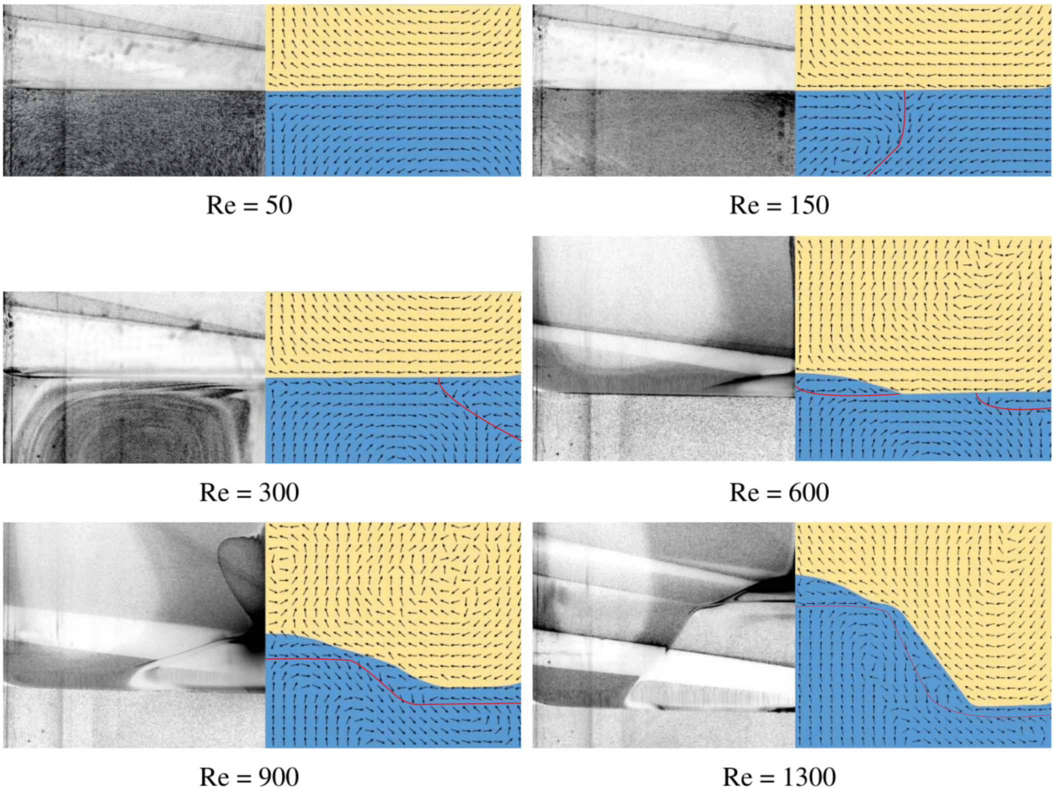

FIG. 10. Photos (left) and PIV images of the meridional flow (right) near the interface with a better resolution than that in Fig. 9.

F. Scenario of flow topological transformations as TCL develops

To highlight the main new results of this work, Fig. 11 schematically shows changes in the flow topology, as the TCL develops. Figure 11(a) depicts the topology at Re = 300. CC denotes the centrifugal circulation. The subscripts "o" and "g" mean "oil" and "glycerin," respectively. The interface is depicted by the thick dark (red) and light (yellow) curves.

Below the light curve, there is a thin region of glycerin anticentrifugal circulation (AC_{g1}), attached to the sidewall and radially extending from the sidewall to nearly a half of the cylinder radius in Fig. 11(a). AC_{g1} serves as a fluid bearing separating CC_o and CC_g.

A counterintuitive feature is that CC_o and CC_g are not separated along the near-axis part of the interface, depicted by the dark (red) curve in Fig. 11(a). There is a slip and a counterflow near this part of interface: the oil moves toward the axis while the glycerin moves away from the axis.

Such a discontinuity of the radial velocity at the interface can occur due to the density jump—glycerin density being larger than the oil density—and due to swirl—the centrifugal force pushes to the periphery glycerin more strongly than oil. For a slow rotation, swirl rapidly decays downward and the effect of the centrifugal force on the glycerin flow is negligible compared with the effect of CC_o. Accordingly, there is no counterflow near the interface, as Fig. 4(b) illustrates. However, as the rotation intensifies, the strengthened centrifugal force reverses the glycerin radial velocity, making it directed to the periphery below the near-axis part of the interface, as Figs. 4(c)–4(e) show. This reversal generates CC_g, which eventually occupies the most of the glycerin domain, as Fig. 11(a) illustrates. Some other features of the slip phenomenon are discussed in Ref. [22].

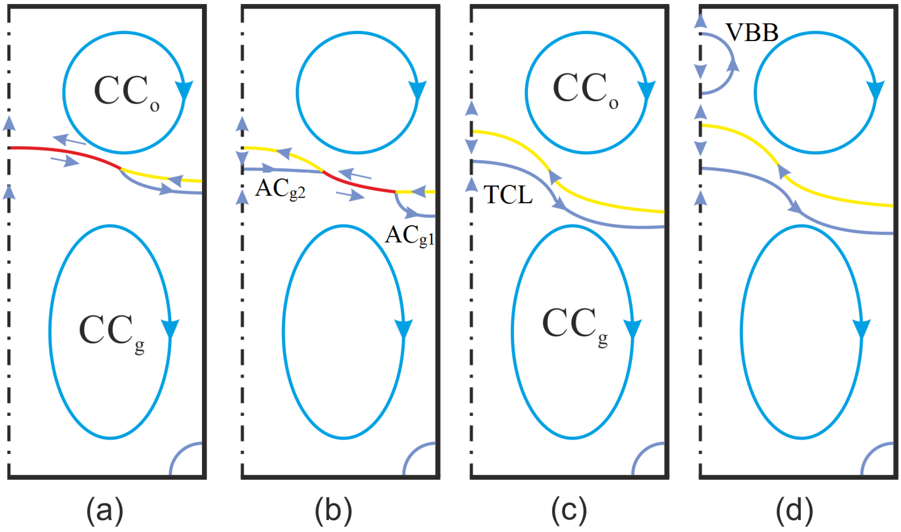

FIG. 11. Schematic of changes in the flow topology as TCL develops: (a) Re = 300, (b) Re = 400, (c) Re = 650, and (d) Re = 700.

As the rotation further intensifies, the second reversal of the glycerin radial velocity occurs and one more region of anticentrifugal circulation (AC$_{g2}$) emerges near the interface-axis intersection, as Fig. 11(b) illustrates. This topological transformation of the lower-fluid flow has not been recognized in prior studies. Its mechanism might be the following.

The rising part of CC$_g$ transports glycerin from the bottom vicinity, where the angular momentum of glycerin is small, along the axis toward the interface. In addition, CC$_g$ blocks the diffusion of the angular momentum from oil to glycerin across the interface near the axis. These two factors—the transport and blockage—weaken the swirl and therefore the centrifugal circulation of glycerin near the interface-axis intersection. In contrast, the oil flow, converging to the axis near the interface, speeds up, entrains the adjacent glycerin, and reverses the glycerin radial velocity. Now the convergence effect overcomes the swirl effect near the axis.

The counterflow of oil and glycerin only remains near the middle part of the interface depicted by the thick dark (red) curve in Fig. 11(b) where the centrifugal force is maximal. As Re further increases, this middle part shrinks and disappears, and AC$_{g1}$ and AC$_{g2}$ meet and merge, forming the TCL attached to the entire interface from below, as Fig. 11(c) illustrates.

The next flow topological transformation is the appearance of the VBB in the oil flow as Fig. 11(d) illustrates. For larger Re, the VBB disappears and the flow topology returns to that shown in Fig. 11(c). These two topological changes of the upper-fluid flow—the appearance and disappearance of the VBB—do not affect the TCL topology which remains invariant up until the flow becomes unsteady and three-dimensional for Re $>$ 1400.

IV. CONCLUSION

This paper demonstrates the first experimental evidence of a TCL developing near the interface of two swirling immiscible fluids. The TCL has been predicted in a number of numerical simulations, but has not been experimentally detected because steady axisymmetric motions of the lower fluid were too slow to clearly visualize and/or to measure. The current study solves this problem by replacing water, used in the previous experiments and simulations, with a glycerin-water solution for the lower fluid. The solution viscosity is larger than the water viscosity by two orders of magnitude, which allows for detecting both velocities and flow patterns of the lower fluid. In order to further improve the signal-to-noise ratio, we also apply averaging of 200 PIV images at a fixed Re.

This advanced experimental technique allows for uncovering a number of the flow topological transformations as the rotation speed (Re) increases. The main result is that the TCL does develop, but in a way that is different from that predicted by the numerical simulations.

First, a new cell of the centrifugal circulation emerges in the lower fluid near the interface-axis intersection. This cell expands downward and eventually occupies almost the entire lower-fluid domain (Sec. III A). This contradicts the simulations where the cell emerges near the bottom and expands upward.

Second, a new cell of the anticentrifugal circulation emerges in the lower fluid near the interface-axis intersection. Third, the new cell merges with the remnants of the initial anticentrifugal circulation, and together, they form a TCL attached to the entire interface from below (Sec. III B).

Fourth, a cell of the anticentrifugal circulation (vortex breakdown bubble) emerges and disappears in the upper fluid (Sec. III C). Fifth, a strong jetlike flow, forming along the TCL's lower boundary, radially diverges from the axis, hits the interface, and thus contributes to the development of the interface's bell shape (Sec. III D).

These flow metamorphoses are uncovered with the help of photos, velocity measurements along the axis and near the interface, and PIV images of meridional motion (Sec. III E). The TCL serves as a liquid bearing separating the bulk centrifugal circulations of the upper and lower fluids (Fig. 11). The TCL is a region of high meridional velocity and shear. The flow features, revealed in these experiments, are of fundamental interest and can be important for applications in bioreactors.

ACKNOWLEDGMENT

This work was carried out under state contract with IT SB RAS (AAAA-A17-117030910025-7), partial support of experimental part of this study from the Russian Foundation for Basic Research (Project No. 18-08-00508) is gratefully acknowledged.

[1] Yu. A. Ramazanov, V. I. Kislykh, I. P. Kosyuk, N. V. Bakuleva, and V. V. Shchurikhina, Industrial production of vaccines using embryonic cells in gas-vortex gradient-less bioreactors, in *New Aspects of Biotechnology and Medicine*, edited by A. M. Egorov (Nova Scientific Books, New York, 2007), pp. 87–91.
[2] K. Y. S. Liow, G. Thouas, B. T. Tan, M. C. Thompson, and K. Hourigan, Modelling the transport of momentum and oxygen in an aerial-disk driven bioreactor used for animal tissue or cell culture, IFMBE Proc. **23**, 1672 (2008).
[3] K. Y. S. Liow, B. T. Tan, G. Thouas, and M. C. Thompson, CFD modeling of the steady-state momentum and oxygen transport in a bioreactor that is driven by an aerial rotating disk, Mod. Phys. Lett. B **23**, 121 (2009).
[4] D. Lo Jacono, M. Nazarinia, and M. Brøns, Experimental vortex breakdown topology in a cylinder with a free surface, Phys. Fluids **21**, 111704 (2009).
[5] M. A. Herrada and V. N. Shtern, Patterns of a creeping water-spout flow, J. Fluid Mech. **744**, 65 (2014).
[6] A. Balci, M. Brons, M. A. Herrada, and V. N. Shtern, Vortex breakdown in a truncated conical bioreactor, Fluid Dyn. Res. **47**, 065503 (2015).
[7] A. Balci, M. Brons, M. A. Herrada, and V. N. Shtern, Patterns of a slow air-water flow in a semispherical container, Eur. J. Mech. B Fluids **58**, 1 (2016).
[8] A. Balci, M. Brons, M. A. Herrada, and V. N. Shtern, Bifurcations of a creeping air-water flow in a conical container, Theor. Comput. Fluid Dyn. **30**, 485 (2016).
[9] S. Fujimoto and Y. Takeda, Topology changes of the interface between two immiscible liquid layers by a rotating lid, Phys. Rev. E **80**, 015304(R) (2009).

[10] J.-C. Tsai, C.-Y. Tao, Y.-C. Sun, C.-Y. Lai, K.-H. Huang, W.-T. Juan, and J.-R. Huang, Vortex-induced morphology on a two-fluid interface and the transitions, Phys. Rev. E **92**, 031002(R) (2015).

[11] L. Carrión, M. A. Herrada, and V. N. Shtern, Topology and stability of a water-soybean-oil swirling flow, Phys. Rev. Fluids **2**, 024702 (2017).

[12] L. Carrión, M. A. Herrada, and V. N. Shtern, Topology changes in a water-oil swirling flow, Phys. Fluids **29**, 032109 (2017).

[13] I. V. Naumov, B. R. Sharifullin, and V. N. Shtern, Capillary hysteresis in a confined swirling two-fluid flow, J. Eng. Thermophys., **26**, 391 (2017).

[14] I. V. Naumov, B. R. Sharifullin, and V. N. Shtern, Hysteresis in a swirling two-fluid flow, J. Phys: Conf. Ser. **899**, 032015 (2017).

[15] M. A. Herrada, V. N. Shtern, and J. Lopez-Herrera, Vortex breakdown in a water-spout flow, Phys. Fluids **25**, 093604 (2013).

[16] L. Carrión, M. A. Herrada, and V. N. Shtern, Instability of a water-spout flow, Phys. Fluids **28**, 034107 (2016).

[17] I. V. Naumov, M. A. Herrada, B. R. Sharifullin, and V. N. Shtern, Hysteretic growth and decay of a waterspout column, Phys. Rev. Fluids **3**, 024701 (2018).

[18] H. K. Moffatt, Viscous and resistive eddies near a sharp corner, J. Fluid Mech. **18**, 1 (1964).

[19] V. N. Shtern, M. M. Torregrosa, and M. A. Herrada, Effect of swirl decay on vortex breakdown in a confined steady axisymmetric flow, Phys. Fluids **24**, 043601 (2012).

[20] M. A. Herrada, V. N. Shtern, and M. M. Torregrosa, The instability nature of Vogel-Escudier flow, J. Fluid Mech. **766**, 590 (2015).

[21] M. P. Escudier, Vortex breakdown: Observations and explanations, Progr. Aerospace Sci. **25**, 189 (1988).

[22] I. V. Naumov, M. A. Herrada, B. R. Sharifullin, and V. N. Shtern, Slip at the interface of a two-fluid swirling flow, Phys. Fluids **30**, 074101 (2018).